Journal of Materials Chemistry C

ROYAL SOCIETY OF CHEMISTRY

PAPER

View Article Online
View Journal | View Issue

Cite this: J. Mater. Chem. C, 2025, 13, 655

Synthesis and electron-transporting properties of phenazine bisimides†

Keita Tajima,[a] Taito Moribe,[a] Kyohei Matsuo,[b] Hiroko Yamada,[b]* Shu Seki,[c]* Seiya Yokokura,[d] Toshihiro Shimada,[d] Norihito Fukui[ae]* and Hiroshi Shinokubo[a]*

Received 2nd August 2024,
Accepted 28th October 2024

DOI: 10.1039/d4tc03306j

rsc.li/materials-c

The dual incorporation of imide substituents and imine-type nitrogen atoms into π-systems represents an emerging guideline for the design of robust and high-performance n-type semiconductors. Herein, we have adapted this strategy to a simple molecular motif: anthracene, and thus synthesized phenazine bisimides (PzBIs). PzBIs exhibit superior electron affinity compared to anthracene bisimide and phenazine due to the presence of two types of functional electron-withdrawing units. The existence of imine-type nitrogen atoms in PzBI leads to the formation of two-dimensionally extended brickwork arrangements while anthracene bisimide forms one-dimensionally slipped-stacked arrays. Consequently, the electron mobility of the vacuum-deposited film of *N*,*N*′-dicyclohexyl PzBI is ten times higher than that of the corresponding anthracene bisimide. Furthermore, the OFET device of *N*,*N*′-bisheptafluorobutyl PzBI exhibits good air persistency, and its intrinsic electron mobility has been estimated to be approximately 0.7 $cm^2 V^{-1} s^{-1}$ by the time-resolved microwave conductivity measurement. The current study demonstrates that the dual incorporation strategy endows even a simple and small π-system with good performance as an n-type semiconductor.

Introduction

Organic semiconductors have been actively explored for the development of advanced electronic materials due to their mechanical flexibility, lightweight, and high designability. Recent advances in the design of p-type organic semiconductors have furnished various promising molecules for practical applications.[1–8] On the other hand, the development of efficient n-type organic semiconductors has still lagged. Considering the dual use of both p-type and n-type semiconductors is necessary for several advanced applications such as logic gate transistors and photovoltaics, the establishment of a general and reliable guideline for the molecular design of high-performance n-type semiconductors is desirable.[9–13]

One traditional strategy for the design of n-type organic semiconductors is the introduction of electron-withdrawing imide substituents on the periphery of aromatic molecules, as seen in naphthalene diimide (NDI) and perylene bisimide (PBI).[14–18] The advantage of this approach is the high tunability of the solubility and solid-state arrangement by the substituents on the nitrogen atoms. Another strategy is the incorporation of electronegative imine-type nitrogen atoms, which significantly deepens the lowest unoccupied molecular orbital (LUMO) level of the parent π-systems.[19–21] Furthermore, the hydrogen-bond-accepting ability of the incorporated imine-type nitrogen atoms allows the control of the intermolecular arrangement.

The dual incorporation of imide substituents and imine-type nitrogen atoms represents an emerging strategy for the design of robust and high-performance n-type semiconductors.[22–33] The representative molecules based on this strategy are listed in Fig. 1. Jenekhe and co-workers have synthesized heterocyclic diimides **1**, which exhibits a maximum carrier mobility of 0.12 $cm^2 V^{-1} s^{-1}$ under vacuum conditions.[22] Okamoto and co-workers have reported that benzo[*de*]isoquinolino[1,8-*gh*]quinolinetetracarboxylic diimide (BQQDI) **2** shows high electron mobility of 3.0 $cm^2 V^{-1} s^{-1}$ and excellent air-durability.[23,24] We have also contributed to this research field with acridino[2,1,9,8-*klmna*]acridine bisimide (AABI) **3**, whose single-crystal organic field-effect

[a] Department of Molecular and Macromolecular Chemistry, Graduate School of Engineering and Integrated Research Consortium on Chemical Sciences (IRCCS), Nagoya University, Furo-cho, Chikusa-ku, Nagoya 464-8603, Japan. E-mail: fukui@chembio.nagoya-u.ac.jp, hshino@chembio.nagoya-u.ac.jp
[b] Institute for Chemical Research, Kyoto University, Gokasho, Uji, Kyoto 611-0011, Japan. E-mail: hyamada@scl.kyoto-u.ac.jp
[c] Department of Molecular Engineering, Graduate School of Engineering, Kyoto University, Nishikyo-ku, Kyoto 615-8510, Japan. E-mail: seki@moleng.kyoto-u.ac.jp
[d] Graduate School of Chemical Sciences and Engineering, Hokkaido University, Kita 13 Nishi 8, Kita-ku, Sapporo 060-8628, Japan
[e] PRESTO, Japan Science and Technology Agency (JST), Kawaguchi, Saitama 332-0012, Japan

† Electronic supplementary information (ESI) available. CCDC 2348426–2348428. For ESI and crystallographic data in CIF or other electronic format see DOI: https://doi.org/10.1039/d4tc03306j

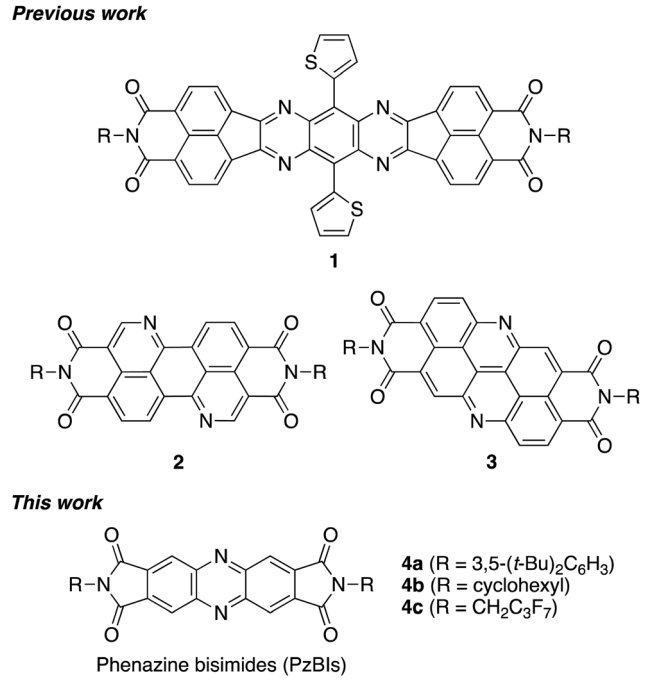

Fig. 1 Imide-functionalized electron-accepting π-systems that contain imine-type nitrogen atoms.

transistor (OFET) device achieved an electron mobility of 0.90 $cm^2 V^{-1} s^{-1}$.[25]

Herein, we have applied the dual incorporation strategy to anthracene, and thus designed phenazine bisimide (PzBI). The structure of PzBI is simpler than those of previously reported nitrogen-incorporated imide-functionalized molecules including **1–3**.[22–33] The structural simplicity should be advantageous for deeply understanding the structure–property relationship of this molecular design. To date, two imide-functionalized anthracene derivatives **5** and **6** have been reported (Fig. 2). Compound **5** contains imide groups at the zigzag edges of the anthracene core,[34,35] while **6** has imide-substituents at the short sides of the molecule.[36,37] The reduction potentials of **5** and **6** are −1.02 V and −1.69 V (*vs.* Fc/Fc^+), respectively, and thus higher than that of anthracene (−2.91 V). Compound **6** functions as an organic n-type semiconductor with a maximum electron mobility (μ) of 1.0×10^{-2} $cm^2 V^{-1} s^{-1}$. However, anthracene derivatives that contain both nitrogen atoms and imide substituents have not yet been reported.

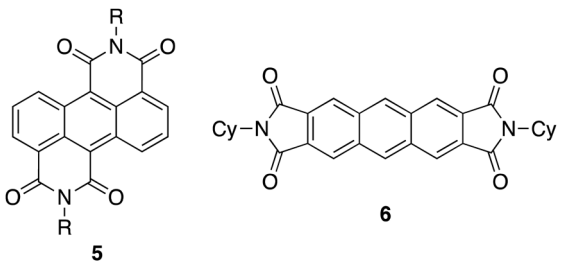

Fig. 2 Anthracene diimides **5** and **6**.

Results and discussion

Synthesis

The synthetic procedure for PzBIs **4a–4c** is shown in Scheme 1. The reduction of diethyl 4-nitrophthalate **7** with $SnCl_2$ and HCl aq. afforded diethyl 4-aminophthalate **8** in 90% yield. The iodination of **8** with *N*-iodosuccinimide (NIS) proceeded at the 5-position to provide **9** in 57% yield. The dimerization of **9** *via* a palladium-catalyzed Buchwald–Hartwig amination[38,39] and spontaneous dehydrogenation furnished the ester-functionalized phenazine derivative **10** in 63% yield. The hydrolysis of **10** generated tetracarboxylic acid **11** in 87% yield. The subsequent dehydration[40] of **11** with trifluoroacetic anhydride afforded acid anhydride **12** in 80% yield, which was treated with three different amines to afford the corresponding PzBIs **4a** (*R* = 3,5-di-*tert*-butylphenyl), **4b** (*R* = cyclohexyl), and **4c** (*R* = 2,2,3,3,4,4,4-heptafluorobutyl) in 22%–63% yields. The smaller isolated yield of **4c** (22%) compared to **4a** (63%) and **4b** (61%) is due to the loss by the recrystallization.

Optical properties

The UV/vis absorption and emission spectra of PzBI **4a** are shown in Fig. 3. In CH_2Cl_2 at room temperature, PzBI **4a** exhibits weak and ill-resolved absorption bands around 350–450 nm. PzBI **4a** emits orange fluorescence with a small quantum yield (Φ = 0.02) and a lifetime of 0.5 ns. These parameters afford a radiative decay rate constant (k_r) of 4.6×10^7 s^{-1} and a non-radiative decay constant (k_{nr}) of 2.0×10^9 s^{-1}. A frozen (77 K) 2-methyltetrahydrofuran solution of **4a** showed red phosphorescence in 600–750 nm with a lifetime of 43 ms. The generation of a photoexcited triplet species was further corroborated by the transient absorption spectra (Fig. S43, ESI†). Density functional theory (DFT) calculations at the CAM-B3LYP/6–31+G(d,p) level demonstrated that the lowest-energy absorption of PzBI is mainly attributable to the n–π* transition involving the lone pair of the doped imine-type nitrogen. The n–π* nature of the S_0–S_1 transition in PzBI accelerates ISC. Indeed, *N*-cyclohexyl PzBI **4b** is non-emissive, while cyclohexyl-substituted anthracene bisimide **6** shows an intense emission (Φ = 0.54) with a lifetime of 8.6 ns (Fig. S44, ESI†).[37] These results indicate that the effective ISC of **4a** originates from the doped imine-type nitrogen atoms.

Electrochemical properties

Cyclic voltammetry and differential pulse voltammetry were conducted on PzBI **4b** and anthracene bisimide **6** in CH_2Cl_2 using 0.1 M Bu_4NPF_6 as the supporting electrolyte and $Ag/AgNO_3$ as the reference electrode (Fig. 4). All potentials are given relative to the Fc/Fc^+ couple as an external standard. PzBI **4b** exhibits two reversible reduction waves at −1.07 V and −1.63 V. The first reduction potential of **4b** is shifted to significantly higher voltages relative to those of anthracene bisimide **6** (−1.74 V)[36,37] and phenazine (−1.83 V).[41] The first reduction potential of **4b** (−3.8 eV *vs.* vacuum) is close to the criterion for air-stable electron-transporting materials (< −4.0 eV *vs.* vacuum).[13,42] These results indicate that the incorporation of both sp^2-hybridized nitrogen atoms and imide substituents effectively enhances the electron-accepting character of anthracene. This dual stabilization of the LUMO

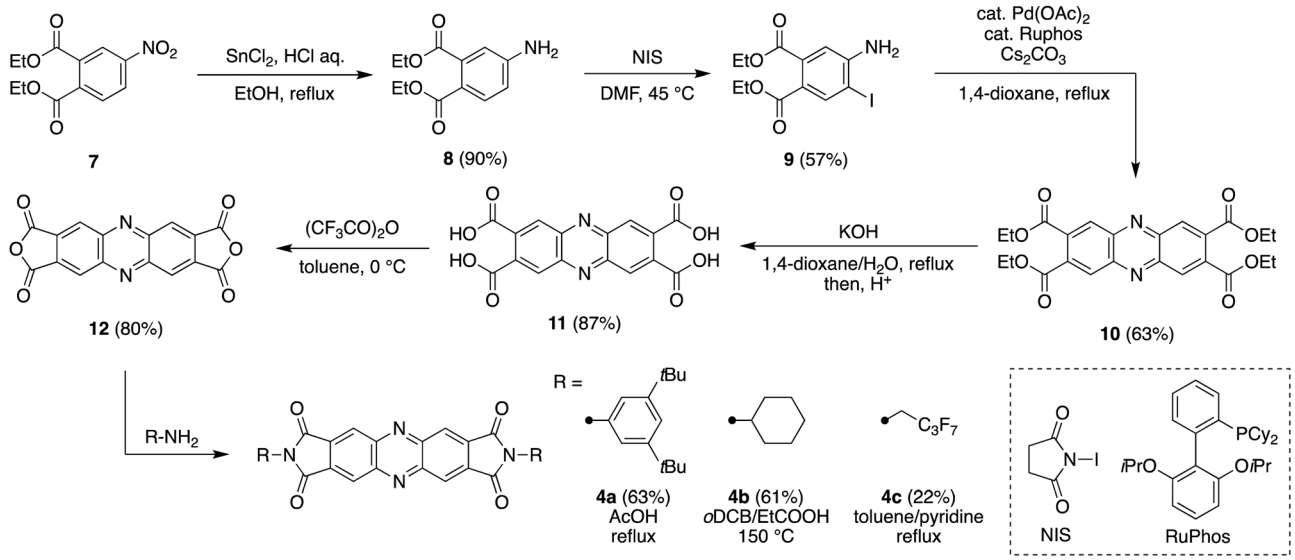

Scheme 1 Synthesis of the PzBIs **4a–4c**.

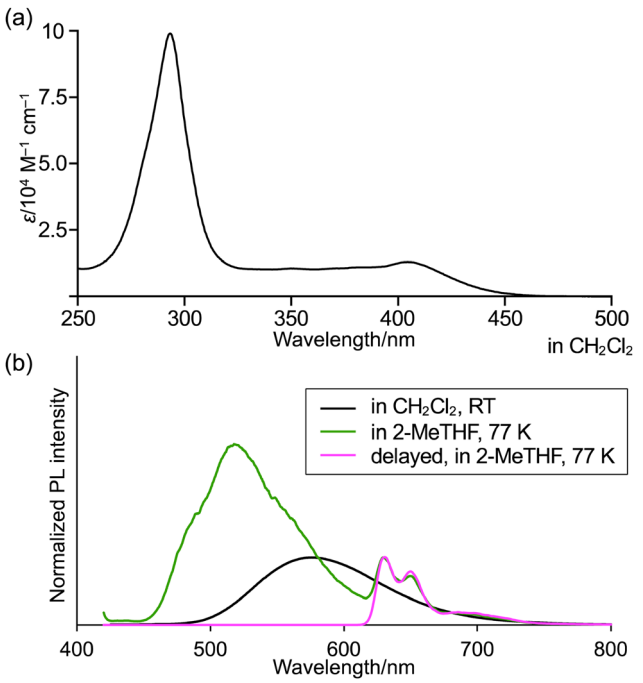

Fig. 3 (a) UV/vis absorption spectra of **4** in CH_2Cl_2. (b) Emission spectra of **4a** under different measurement conditions.

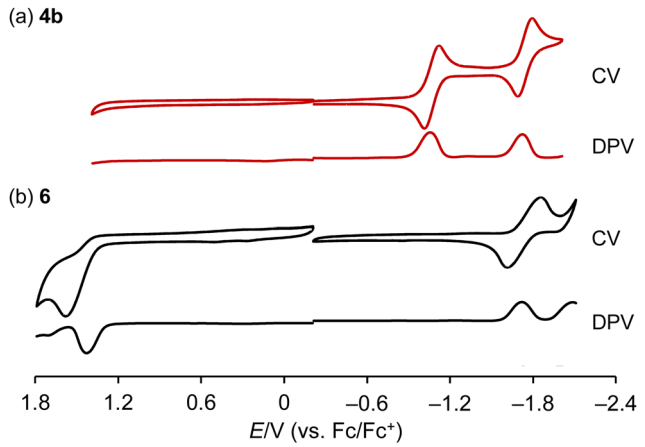

Fig. 4 Cyclic and differential pulse voltammograms of (a) **4b** and (b) **6** in CH_2Cl_2.

level has also been confirmed by the density functional theory (DFT) calculations (Fig. S42, ESI†). Other derivatives **4a** and **4c** also exhibited two reduction waves (**4a:** −0.99 and −1.60 V; **4c:** −0.88 and −1.52 V), which are comparable to those of **4b** (Fig. S45 and S46, ESI†).

X-ray diffraction analyses

The solid-state structures of **4b** and **4c** were unambiguously determined *via* single-crystal X-ray diffraction analysis (Fig. 5a and Fig. S28, ESI†). High-quality crystals of **4c** were prepared using the naphthalene flux method.[43–45] In the single crystal, *N*,*N*′-dicyclohexyl PzBI **4b** adopts a planar structure with a small mean-plane deviation (MPD), defined by 24 atoms in the π-core, of 0.09 Å. The C–N bond lengths at the central pyrazine unit (1.346(2) and 1.339(2) Å) are typical for pyridinic sp^2-hybridized nitrogen atoms. The C–N–C bond angle (116.5(1)°) is narrower than that of an ideal hexagon (120°) due to the imine-type nitrogen atoms. The harmonic oscillator model of aromaticity (HOMA) value[46] for the central pyrazine subunit (0.79) suggests local aromatic character. The structural features of *N*,*N*′-bis(2,2,3,3,4,4,4-heptafluorobutyl) PzBI **4c** are similar to those of **4b** (Fig. S28, ESI†).

The crystal packing of PzBIs **4b** and **4c** is characterized by a brickwork arrangement with interplanar distances of 3.15 Å and 3.05 Å, respectively (Fig. 6). These interplanar distances are remarkably shorter than the sum of the van der Waals radii of

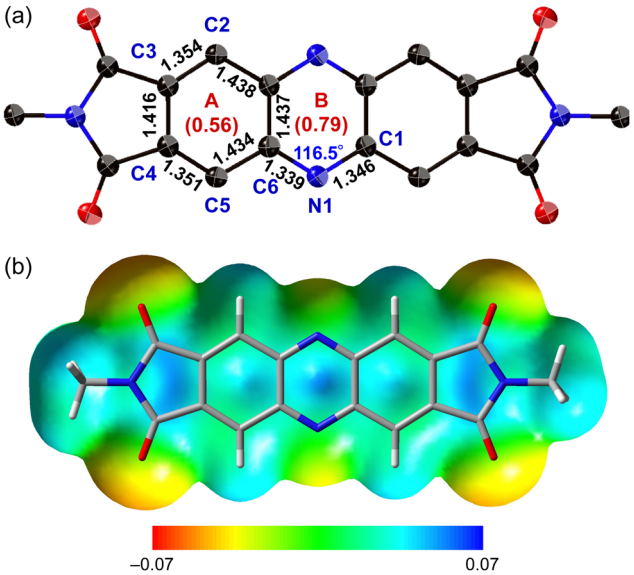

Fig. 5 (a) Crystal structure of **4b** with thermal ellipsoids at 50% probability. Hydrogen atoms and substituents on imide groups are omitted for clarity. The value in parentheses shows the HOMA value. (b) Calculated ESP map of *N*,*N*′-dimethyl PzBI at the B3LYP/6-31G+(d,p) level.

the carbon atoms (3.4 Å), which could be attributed to the decreased exchange repulsion in these electron-accepting π-systems. Anthracene bisimide **6** forms a different packing structure in which one-dimensionally slipped-stacked arrays align in alternating parallel and inverted arrangements (Fig. 6e). The combined results of the following analysis suggest that the preferential formation of the brickwork packing in PzBIs **4b** and **4c** originates from the cooperative effect of the imide substituents and imine-type nitrogen atoms. A Hirshfeld surface analysis[47] of PzBIs **4b** and **4c** indicates the presence of hydrogen bonding between the aromatic C–H protons and the carbonyl groups (Fig. 6b and d). While hydrogen bonding between other aromatic C–H protons and the imine-type nitrogen atoms is negligible, the C–H units are adjacent to the imine-type nitrogen atoms. The hypothetical replacement of these imine-type nitrogen atoms with C–H units can be expected to induce strong steric repulsion, which is likely the origin of the observed slipped-stacked arrangements for anthracene bisimide **6**. Furthermore, the calculated electrostatic potential (ESP) map of *N*,*N*′-dimethyl PzBI demonstrates the alternate distribution of electropositive/electronegative sites along the longitudinal axis, which is perforable to minimize the misalignment along this axis (Fig. 5b and Fig. S40, ESI†).[23,24]

Electron-transporting ability

We fabricated vacuum-deposited OFET devices based on **4b** and **4c**. For that purpose, an Al_2O_3/SiO_2 dielectric layer on a Si wafer was treated with a self-assembled monolayer of 12-cyclohexyldodecylphosphonic acid (CDPA),[48] before a thin layer of **4b** or **4c** was vacuum-deposited on the substrate (*ca.* 5×10^{-4} Pa; 0.03 nm s^{-1}). Then, gold electrodes were vacuum-deposited on the active layer as the source and drain electrodes (Fig. S29, ESI†). An atomic-force-microscopy (AFM) analysis showed that each substrate had a rough surface with tiny submicron grains (Fig. S30, ESI†). Out-of-plane X-ray diffraction analysis of a thin film made from **4b** revealed a peak at 4.7°, corresponding to a distance of 18.6 Å, which is comparable to the *c* axis (18.5347(6) Å) of the unit cell (Fig. S31, ESI†). These results suggest that PzBI **4b** adopts an edge-on arrangement on the substrate surface, which is preferable for effective carrier transport in OFET devices.[49] On the other hand, the vacuum-deposited film of **4c** did not show any obvious peaks due to its lower crystallinity.

The properties of the OFET devices were measured at room temperature *in vacuo* (*ca.* 3×10^{-1} Pa). The fabricated OFET devices exhibited typical n-type behavior (Fig. 7 and Fig. S33 and S34 and Tables S1–S3, ESI†) (Table 1). In the case of *N*,*N*′-dicyclohexyl PzBI **4b**, the maximum and average electron mobilities are 9.9×10^{-2} cm^2 V^{-1} s^{-1} and $(4.6 \pm 2.4) \times 10^{-2}$ cm^2 V^{-1} s^{-1}, respectively. This maximum electron

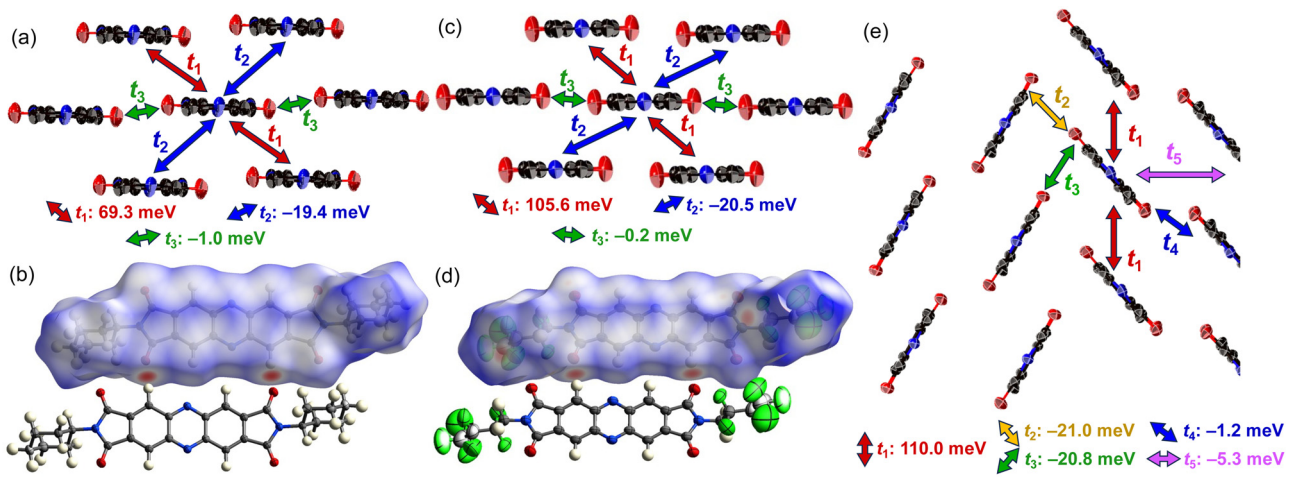

Fig. 6 Crystal structures of **4b**, **4c**, and **6** with thermal ellipsoids at 50% probability. (a) Side view of the crystal packing of **4b**. (b) Hirshfeld surface analysis of **4b**. (c) Side view of the crystal packing of **4c**. (d) Hirshfeld surface analysis of **4c**. (e) Side view of the crystal packing of **6**. In (a) and (c), the hydrogen atoms and substituents on the imide groups are omitted for clarity; arrows in (a), (c), and (e) indicate the direction of the transfer integrals.

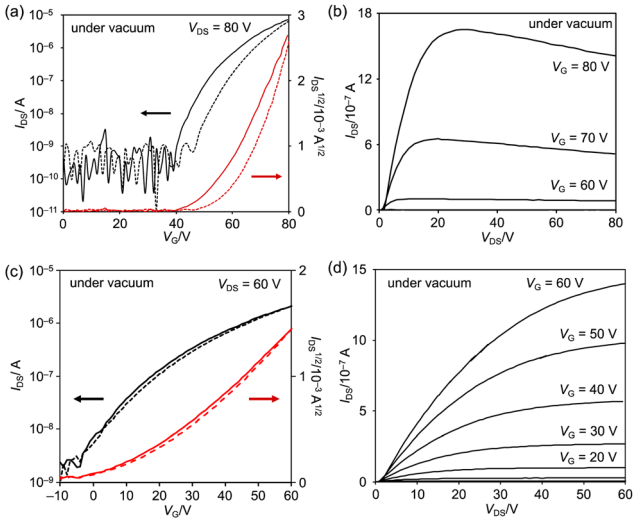

Fig. 7 Thin-film OFET properties of **4b** and **4c** under vacuum conditions; (a) transfer characteristics of **4b**; (b) output characteristics of **4b**; (c) transfer characteristics of **4c**; (d) output characteristics of **4c**.

mobility of **4b** is approximately ten times higher than that of anthracene bisimide **6** (1.0×10^{-2} cm^2 V^{-1} s^{-1}). The electron mobility of *N*,*N*′-bisheptafluorobutyl PzBI **4c** is up to 8.2×10^{-3} cm^2 V^{-1} s^{-1}, which is smaller than that of **4b** due to the low crystallinity of the thin films of **4c** (Fig. S31, ESI†). On the other hand, the film of **4c** exhibits superior air durability compared to that of **4b**, reflected in the small hysteresis in transfer characteristics and the relatively suppressed drop of electron mobility under air. The enhancement of air persistency by fluoroalkyl groups has been reported previously.[50,51]

As heptafluorobutyl derivative **4c** exhibited low electron mobility when incorporated in an OFET device, we estimated its intrinsic electron-transporting ability using time-resolved microwave conductivity (TRMC)[52] measurements (Fig. S35–S37, ESI†). Electrodeless photocarrier injection was performed upon excitation at 355 nm, where the electronic transitions of the series of molecules tested are minimal, to ensure homogeneous photocarrier distribution in their crystalline states. The major charge-carrier species were determined to be electrons given that the transient conductivity decreased significantly upon exposure to SF_6 gas (Fig. S37, ESI†). To estimate the carrier mobility, the direct-current mode photocurrent was measured using a gold electrode on a glass substrate. For that purpose, **4c** was cast onto gold electrodes with a 5 μm gap and excited at 355 nm with laser pulses of 4.1×10^{15} photons cm^{-2}. The photocurrent of **4c** was proportional to the applied bias voltage (Fig. S36, ESI†) and the quantum yield of the carrier generation was estimated to be 2.3×10^{-4}. Moreover, the photoconductivity ($\Phi\Sigma\mu$) of **4c** was determined to be 1.5×10^{-4} cm^2 V^{-1} s^{-1} based on the modulated excitation density at 355 nm of 3.6×10^{15} photons cm^{-2}. Finally, the minimum mobility in the crystalline forms was estimated to be μ = 0.7 cm^2 V^{-1} s^{-1}, suggesting highly conductive pathways in crystalline domains.[52,53] We also conducted the TRMC measurements for **4b** and **6**, which indicates that nitrogen-doped species **4b** exhibits one order of magnitude higher conductivity than **6** (Fig. S38, ESI†).

Table 1 Vacuum-deposited OFET characteristics in the saturated regions of **4b** and **4c**

	μ_{max} [cm^2 V^{-1} s^{-1}]		$\mu_{average}$ [cm^2 V^{-1} s^{-1}]	
	Vacuum	Air	Vacuum	Air
4b	9.9×10^{-2}	6.4×10^{-3}	$(4.6 \pm 2.4) \times 10^{-2}$	$(2.2 \pm 0.8) \times 10^{-3}$
4c	8.2×10^{-3}	3.5×10^{-3}	$(5.7 \pm 2.9) \times 10^{-3}$	$(2.6 \pm 1.7) \times 10^{-3}$

To explore why PzBI exhibits better electron-transporting properties than anthracene bisimide, we conducted DFT calculations to estimate the reorganization energies, λ, upon electron injection at the (U)B3LYP/6-31+G(d,p) level. The obtained λ value of *N*,*N*′-dimethyl PzBI (119 meV) is smaller than that of *N*,*N*′-dimethyl anthracene bisimide (268 meV). The small λ value of PzBI is advantageous for the efficient electron-transport according to the hopping model.[54] The electron injection causes the elongation of carbonyl C–O bonds and the shortening of the C–C bonds between the carbonyl groups and fused benzene units in both anthracene bisimide and PzBI. These displacements are more significant in anthracene bisimide rather than PzBI (C–O: 0.012 Å *vs.* 0.008 Å; C–C: 0.031 Å *vs.* 0.015 Å) (Fig. S41, ESI†). Furthermore, the bond displacements in the imide-substituted benzene rings are more significant in anthracene bisimide (up to 0.030 Å) rather than PzBI (up to 0.019 Å). These results suggest that the considerable reorganization energy of anthracene bisimide is caused by the predominant delocalization of the injected electron on the peripheral carbonyl groups, which associates with the deformation of local 6π-conjugation in the imide-substituted benzene rings. In contrast, the injected electron in PzBI can be stabilized by the two electronegative nitrogen atoms in the phenazine core, which suppresses the bond displacement upon electron injection.

We also calculated the transfer integrals, *t*, between the LUMOs of **4b**, **4c**, and **6** in their crystal-packing structures by the DFT method at the PBEPBE/6-31G(d) level (Fig. 5). Both **4b** and **4c** exhibit similar trends. The *t* value in the stacking direction is sufficiently high (**4b**: 69.3–19.4 meV; **4c**: 105.6–20.5 meV) to facilitate the construction of two-dimensional conducting pathways. In contrast, while anthracene bisimide **6** exhibits a large transfer integral along the stacking direction (110.0 meV), the carrier transport along the perpendicular direction is disrupted by the parallel alignment of the slipped-stacked columns due to the significantly small transfer integrals (up to 5.3 meV). Consequently, **6** has only a one-dimensional conducting pathway, hampering effective carrier transport. These results highlight the effectiveness of the brick-work arrangements of PzBIs for the efficient electron transport.

Redox interconversion

The reduction of **4a** was accomplished by treatment with 1,4-bis(trimethylsilyl)-1,4-dihydropyrazine and MeOH to afford the corresponding *N*,*N*′-dihydro derivative **13** in 89% yield (Scheme 2). The ^{1}H NMR spectrum of **13** shows a signal arising from the NH protons at 8.8 ppm, which disappeared upon adding D_2O. The oxidation of *N*,*N*′-dihydro PzBI **13** with

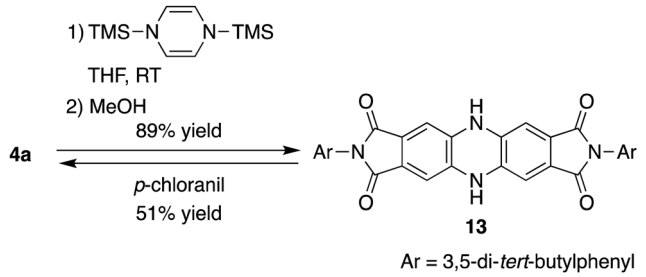

Scheme 2 Redox interconversion between PzBI **4a** and its *N*,*N*′-dihydro derivative **13**.

p-chloranil reversely furnished PzBI **4a** in 51% yield. The absorption of dihydro derivative **13** contains three bands: a sharp and intense peak at 313 nm, a broad band with moderate intensity at 350–450 nm, and a very weak forbidden absorption in the 450–650 nm region (Fig. 8). In addition, **13** is non-emissive. These spectral features are characteristic of an antiaromatic compound.[55,56] The local antiaromaticity of the dihydropyrazine subunit of **13** has been further supported by the DFT calculations: a positive nucleus-independent-chemical-shift (NICS)[57] value (+7.0 ppm) and a counterclockwise ring current in the anisotropy-of-the-induced-current-density (ACID)[58] simulation (Fig. 8, inset).

Conclusions

We have reported the synthesis and properties of three PzBIs **4a–4c**, which represent imide-functionalized anthracene derivatives containing imine-type nitrogen atoms. PzBIs **4** showed excellent electron affinity with a first reduction potential of −1.02 V (*vs.* Fc/Fc$^+$). Vacuum-deposited OFET devices based on cyclohexyl derivative **4b** exhibited n-type semiconducting behavior with an electron mobility of up to 9.9×10^{-2} cm^2 V^{-1} s^{-1}. Time-resolved microwave conductivity measurements revealed that the intrinsic electron mobility of heptafluorobutyl derivative **4c** is approximately 0.7 cm^2 V^{-1} s^{-1}. These values are higher than that of anthracene bisimide **6** (1.0×10^{-2} cm^2 V^{-1} s^{-1}). Considering that the OFET device of **4c** exhibits high air persistency, our results conclude that **4c** is a robust and efficient n-type organic semiconductor. We have rationalized that the superior electron-transporting ability of PzBIs **4b** and **4c** compared to **6** is due to their brickwork-type crystal-packing structures and high electron affinity. Both features originate from the cooperative function of imide-substituents and doped imine-type nitrogen atoms. These results underline the versatility of this molecular design for the development of practical n-type semiconductors.

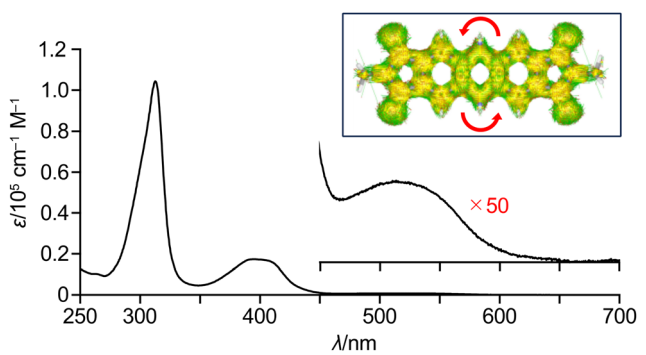

Fig. 8 UV/vis absorption spectra of **13** in CH_2Cl_2. Inset: ACID plot of **13**.

Author contributions

The manuscript was written through the contributions of all authors. All authors have approved of the final version of the manuscript. H. S. and N. F. supervised the project and finalized the manuscript. K. T. performed all the experiments except for the TRMC measurement and wrote the original draft. T. M. collected CV data of compounds **4a** and **4c**. K. M. and H. Y. supported the fabrication of OFET devices and analyzed the results. S. S. conducted the TRMC measurement and analyzed the results. T. S. and S. Y. supported the preparation of single crystals using the naphthalene flux method.

Data availability

All data are available in the main text or the ESI.† Crystallographic data are freely accessible *via* the Cambridge Crystallographic Data Centre (CCDC). Deposition numbers: 2348427 (**4b**); 2348428 (**4c**); 2348426 (**6**).†

Conflicts of interest

There are no conflicts to declare.

Acknowledgements

This work was supported by JSPS KAKENHI grants JP20H05862 (H. S. and N. F.), JP20H05863 (H. S.), JP20H05867 (N. F.), JP22K14663 (N. F.), JP23H03947 (N. F.), JP24K01467 (N. F.), and JP20H05833 (H. Y.) as well as JST PRESTO grant JPMJPR21Q7 (N. F.). The authors would like to thank Dr Yoshitaka Aramaki for the transient-absorption-spectroscopy measurements.

Notes and references

1 M. M. Payne, S. R. Parkin and J. E. Anthony, *J. Am. Chem. Soc.*, 2005, **127**, 8028.
2 M. L. Tang, T. Okamoto and Z. Bao, *J. Am. Chem. Soc.*, 2006, **128**, 16002.
3 H. Ebata, T. Izawa, E. Miyazaki, K. Takimiya, M. Ikeda, H. Kuwabara and T. Yui, *J. Am. Chem. Soc.*, 2007, **129**, 15732.
4 M. J. Kang, I. Doi, H. Mori, E. Miyazaki, K. Takimiya, M. Ikeda and H. Kuwabara, *Adv. Mater.*, 2011, **23**, 1222.
5 K. Bulgarevich, S. Horiuchi and K. Takimiya, *Adv. Mater.*, 2023, **35**, 2305548.
6 T. Okamoto, C. Mitsui, M. Yamagishi, K. Nakahara, J. Soeda, Y. Horise, K. Miwa, H. Sato, A. Yamato, T. Matsushita, T. Uemura and J. Takeya, *Adv. Mater.*, 2013, **25**, 6392.

7 T. Okamoto, C. P. Yu, C. Mitsui, M. Yamagishi, H. Ishii and J. Takeya, *J. Am. Chem. Soc.*, 2020, **142**, 9083.
8 T. Oyama, T. Mori, T. Hashimoto, M. Kamiya, T. Ichikawa, H. Komiyama, Y. S. Yang and T. Yasuda, *Adv. Electron. Mater.*, 2018, **4**, 1700390.
9 J. E. Anthony, A. Facchetti, M. Heeney, S. R. Marder and X. Zhan, *Adv. Mater.*, 2010, **22**, 3876.
10 A. F. Paterson, S. Singh, K. J. Fallon, T. Hodsden, Y. Han, B. C. Schroeder, H. Bronstein, M. Heeney, I. McCulloch and T. D. Anthopoulos, *Adv. Mater.*, 2018, **30**, 1801079.
11 J. Chen, W. Zhang, L. Wang and G. Yu, *Adv. Mater.*, 2023, **35**, 2210772.
12 H. Usta, A. Facchetti and T. J. Marks, *Acc. Chem. Soc*, 2011, **44**, 501.
13 J. Mei, Y. Diao, A. L. Appleton, L. Fang and Z. Bao, *J. Am. Chem. Soc.*, 2013, **135**, 6724.
14 S. V. Bhosale, C. H. Jani and S. J. Langford, *Chem. Soc. Rev.*, 2008, **37**, 331.
15 C. Wang, H. Dong, W. Hu, Y. Liu and D. Zhu, *Chem. Rev.*, 2012, **112**, 2208.
16 F. Würthner and M. Stolte, *Chem. Commun.*, 2011, **47**, 5109.
17 Z. Liu, G. Zhang, Z. Cai, X. Chen, H. Luo, Y. Li, J. Wang and D. Zhang, *Adv. Mater.*, 2014, **26**, 6965.
18 X. Zhan, A. Facchetti, S. Barlow, T. J. Marks, M. A. Ratner, M. R. Wasielewski and S. R. Marder, *Adv. Mater.*, 2011, **23**, 268.
19 Q. Miao, *Adv. Mater.*, 2014, **26**, 5541.
20 U. H. F. Bunz, J. U. Engelhart, B. D. Lindner and M. Schaffroth, *Angew. Chem., Int. Ed.*, 2013, **52**, 3810.
21 X. Xu, Y. Yao, B. Shan, X. Gu, D. Liu, J. Liu, J. Xu, N. Zhao, W. Hu and Q. Miao, *Adv. Mater.*, 2016, **28**, 5276.
22 H. Li, F. S. Kim, G. Ren, E. C. Hollenbeck, S. Subramaniyan and S. A. Jenekhe, *Angew. Chem., Int. Ed.*, 2013, **52**, 5513.
23 T. Okamoto, S. Kumagai, E. Fukuzaki, H. Ishii, G. Watanabe, N. Niitsu, T. Annaka, M. Yamagishi, Y. Tani, H. Sugiura, T. Watanabe, S. Watanabe and J. Takeya, *Sci. Adv.*, 2020, **6**, eaaz0632.
24 S. Kumagai, H. Ishii, G. Watanabe, C. P. Yu, S. Watanabe, J. Takeya and T. Okamoto, *Acc. Chem. Res.*, 2022, **55**, 660.
25 K. Tajima, K. Matsuo, H. Yamada, S. Seki, N. Fukui and H. Shinokubo, *Angew. Chem., Int. Ed.*, 2021, **60**, 14060.
26 K. Tajima, K. Matsuo, H. Yamada, N. Fukui and H. Shinokubo, *Chem. Sci.*, 2023, **14**, 635.
27 R. P. Ortiz, H. Herrera, M. J. Mancheño, C. Seoane, J. L. Segura, P. M. Burrezo, J. Casado, J. T. López Navarrete, A. Facchetti and T. J. Marks, *Chem. – Eur. J.*, 2013, **19**, 12458.
28 Q. Ye, J. Chang, K.-W. Huang, X. Shi, J. Wu and C. Chi, *Org. Lett.*, 2013, **15**, 1194.
29 P. de Echegaray, M. J. Mancheño, I. Arrechea-Marcos, R. Juárez, G. López-Espejo, J. T. López Navarrete, M. M. Ramos, C. Seoane, R. P. Ortiz and J. L. Segura, *J. Org. Chem.*, 2016, **81**, 11256.
30 J. Shao, J. Chang and C. Chi, *Org. Biomol. Chem.*, 2012, **10**, 7045.
31 H. Li, F. S. Kim, G. Ren and S. A. Jenekhe, *J. Am. Chem. Soc.*, 2013, **135**, 14920.
32 C. P. Yu, A. Yamamoto, S. Kumagai, J. Takeya and T. Okamoto, *Angew. Chem., Int. Ed.*, 2023, **62**, e202206417.
33 S. Kumagai, T. Koguma, T. Annaka, C. Sawabe, Y. Tani, H. Sugiura, T. Watanabe, D. Hashizume, J. Takeya and T. Okamoto, *Bull. Chem. Soc. Jpn.*, 2022, **95**, 935.
34 A. R. Mohebbi, C. Munoz and F. Wudl, *Org. Lett.*, 2011, **13**, 2560.
35 S. Katsuta, K. Tanaka, Y. Maruya, S. Mori, S. Masuo, T. Okujima, H. Uno, K. Nakayama and H. Yamada, *Chem. Commun.*, 2011, **47**, 10112.
36 Z. Wang, C. Kim, A. Facchetti and T. J. Marks, *J. Am. Chem. Soc.*, 2007, **129**, 13362.
37 H. Usta, C. Kim, Z. Wang, S. Lu, H. Huang, A. Facchetti and T. J. Marks, *J. Mater. Chem.*, 2012, **22**, 4459.
38 J. F. Hartwig, *Acc. Chem. Res.*, 2008, **41**, 1534.
39 D. S. Surry and S. L. Buchwald, *Chem. Sci.*, 2011, **2**, 27.
40 Y. Ruan, B.-Y. Wang, J. M. Erb, S. Chen, C. M. Hadad and J. D. Badjić, *Org. Biomol. Chem.*, 2013, **11**, 7667.
41 K. Kotwica, I. Wielgus and A. Proń, *Materials*, 2021, **14**, 5155.
42 B. A. Jones, A. Facchetti, M. R. Wasielewski and T. J. Marks, *J. Am. Chem. Soc.*, 2007, **129**, 15259.
43 T. Yanase, H. Tanoguchi, N. Sakai, M. Jin, I. Yamane, M. Kato, H. Ito, T. Nagahama and T. Shimada, *Cryst. Growth Des.*, 2021, **21**, 4683.
44 X. Yang, M. Li, A. Maeno, T. Yanase, S. Yokokura, T. Nagahama and T. Shimada, *ACS Omega*, 2022, **7**, 28618.
45 H. Tanoguchi, T. Yuki, S. Yokokura, T. Yanase, M. Jin, H. Ito, T. Nagahama and T. Shimada, *ACS Appl. Electron. Mater*, 2023, **5**, 6266.
46 T. M. Krygowski and M. K. Cyrański, *Chem. Rev.*, 2001, **101**, 1385.
47 M. A. Spackman and D. Jayatilaka, *CrystEngComm*, 2009, **11**, 19.
48 D. Liu, Z. He, Y. Su, Y. Diao, S. C. B. Mannsfeld, Z. Bao, J. Xu and Q. Miao, *Adv. Mater.*, 2014, **26**, 7190.
49 M. Uno, I. Doi, K. Takimiya and J. Takeya, *Appl. Phys. Lett.*, 2009, **94**, 103307.
50 R. Schmidt, J. H. Oh, Y.-S. Sun, M. Deppisch, A.-M. Krause, K. Radacki, H. Branschweig, M. Könemann, P. Erk, Z. Bao and F. Würthner, *J. Am. Chem. Soc.*, 2009, **131**, 6215.
51 S. Kumagai, C. P. Yu, S. Nakano, T. Annaka, M. Mitani, M. Yano, H. Ishii, J. Takeya and T. Okamoto, *J. Phys. Chem. Lett.*, 2021, **12**, 2095.
52 S. Seki, A. Saeki, T. Sakurai and D. Sakamaki, *Phys. Chem. Chem. Phys.*, 2014, **16**, 11093The spatial size of the local motion (Δx) can be estimated by Einstein–Smoluchowski equation from Kubo's perturbation theory as: $\Delta x = (\mu k_B T f^{-1} e^{-1})^{1/2}$, where k_B, T, f (=9 GHz), and e are Boltzmann constant, temperature, frequency of probing microwave, and elementary charge, respectively. Given the value of μ in **4c** as the highest as 0.7 $cm^2 V^{-1} s^{-1}$, we obtain the estimate of Δx as ~10 nm, securing the motion of charge carriers confined in a crystalline domain in TRMC measurement.
53 Y. Yasutani, A. Saeki, T. Fukumatsu, Y. Koizumi and S. Seki, *Chem. Lett.*, 2013, **42**, 19.
54 V. Coropceanu, J. Cornil, D. A. da Silva Filho, Y. Olivier, R. Silbey and J.-L. Brédas, *Chem. Rev.*, 2007, **107**, 926.

55 S. Cho, Z. S. Yoon, K. S. Kim, M.-C. Yoon, D.-G. Cho, J. L. Sessler and D. Kim, *J. Phys. Chem. Lett.*, 2010, **1**, 895.
56 J. Cao, G. London, O. Dumele, M. von Wantoch Rekowski, N. Trapp, L. Ruhlmann, C. Boudon, A. Stanger and F. Diederich, *J. Am. Chem. Soc.*, 2015, **137**, 7178.
57 P. V. R. Schleyer, C. Maerker, A. Dransfeld, H. Jiao and N. J. R. Van Eikema Hommes, *J. Am. Chem. Soc.*, 1996, **118**, 6317.
58 D. Geuenich, K. Hess, F. Köhler and R. Herges, *Chem. Rev.*, 2005, **105**, 3758.

